CORA Cork Open Research Archive
Cartlann Taighde Oscailte Chorcaí

Title	Propagation of nanopores and formation of nanoporous domains during anodization of n-InP in KOH
Authors	Buckley, D. Noel;Lynch, Robert P.;Quill, Nathan;O'Dwyer, Colm
Publication date	2015-10-01
Original Citation	Buckley, D. N., Lynch, R. P., Quill, N. and O'Dwyer, C. (2015) 'Propagation of Nanopores and Formation of Nanoporous Domains during Anodization of n-InP in KOH', ECS Transactions, 69(14), pp. 17-32. doi: 10.1149/06914.0017ecst
Type of publication	Article (peer-reviewed)
Link to publisher's version	http://ecst.ecsdl.org/content/69/14/17.abstract - 10.1149/06914.0017ecst
Rights	© 2015 ECS - The Electrochemical Society
Download date	2026-11-15 17:48:56
Item downloaded from	https://hdl.handle.net/10468/6459



UCC
University College Cork, Ireland
Coláiste na hOllscoile Corcaigh

Propagation of Nanopores and Formation of Nanoporous Domains during Anodization of n-InP in KOH

D. Noel Buckley, Robert P. Lynch, Nathan Quill, and Colm O'Dwyer

Department of Physics and Energy
Materials and Surface Science Institute, University of Limerick, Ireland.

Anodization of highly doped (10^{18} cm^{-3}) n-InP in 2 – 5 mol dm^{-3} KOH under potentiostatic or potentiodynamic conditions results in the formation of a nanoporous sub-surface region. Pores originate from surface pits and an individual, isolated porous domain is formed beneath each pit in the early stages of anodization. Each such domain is separated from the surface by a thin non-porous layer (typically ~40 nm) and is connected to the electrolyte by its pit. Pores emanate from these points along the <111>A crystallographic directions to form domains with the shape of a tetrahedron truncated symmetrically through its center by a plane parallel to the surface of the electrode. We propose a three-step model of electrochemical pore formation: (1) hole generation at pore tips, (2) hole diffusion and (3) electrochemical oxidation of the semiconductor to form etch products. Step 1 determines the overall etch rate. However, if the kinetics of Step 3 are slow relative to Step 2, then etching can occur at preferred crystallographic sites leading to pore propagation in preferential directions.

INTRODUCTION

In many materials, anodic etching leads to the formation of porous structures. In metals, localized etching may be promoted by the formation of semi-conducting, metal-oxide/hydroxide layers which, due to interlayer forces, may be molded into tubular structures. In semiconductors, localized etching can occur leading to selective removal of material such that the remaining material forms a skeletal structure that encompasses a network of pores. Si, SiC, Ge, Ge/Si alloys, and various II-VI and III-V compounds (including InP) can be made porous in such a manner[1-13].

The morphologies of these pores vary in orientation, frequency of branching, type of infilling and extent of the porous structure. For instance, porous layers form in GaP anodized in aqueous H_2SO_4 solution by the growth of almost hemispherical domains of pores into continuous porous layers[14]. Such domains form due to the radial propagation of their pores from pits in the electrode surface. However, pore propagation can also occur along crystallographic directions and changing the electrode potential can change the propagation direction of these pores. Similar variations in pore morphology are observed in InP and GaAs. In one of the first observations of porous InP formation, pores with triangular cross sections were reported to form along <111> directions when

(111)A-oriented n-InP was anodized in the dark in aqueous HCl via an array of periodic holes in a Si mask.[15] Similar pores in both GaAs and InP anodized in HCl[16] have been observed to propagate along the <111>A directions. At higher potentials, propagation of such pores deviates from the crystallographic directions[17,18] towards the direction of the source of current[19,20] and switching of potential allows alternation between these two regimes of "crystallographically-oriented" (CO) and "current-line-oriented" (CLO) pore propagation.[21]

It is generally accepted that pore propagation in highly doped n-type semiconductors is controlled by hole generation under the influence of a high electric field due to the small radius of curvature at the pore tip. Zhang[22] modeled the relationship between pore-tip shape and electric field in silicon and showed that the electric field at the surface is sufficiently enhanced by the pore-tips curvature to enable substantial tunneling of carriers. This results in significant etching occurring only at pore-tips, allowing continued propagation of these tips into the substrate.

Both chemical and electrochemical etching[23,24] of III-V semiconductors show preferential etching of {111}B planes (*i.e.* group-V-terminated planes). The slowest-etching plane is usually {111}A and so these facets are revealed during etching of InP, GaAs and GaP. Due to the differing etch rates of crystal planes, the formation of tetrahedral etch pits (seen as dove-tailed and v-groove voids, respectively in (011) and $(01\bar{1})$ cross sections) is observed on the (100) surface of III-V semiconductors.[23]

This paper reviews our work[1-3,5,17] on pore propagation and the resulting domain shape in the InP-KOH system. We propose a model[2] based on pore propagation along the <111>A directions to explain the observed structures and domain shapes, and we compare the predictions of the model quantitatively with the experimental observations. We examine why pore propagation is crystallographically oriented even though the etching is controlled by hole generation at pore tips and propose a three-step model[1] based on competitive kinetics between electrochemical reaction and hole diffusion. The model is supported by a variety of SEM and TEM observations of InP electrodes anodized under various conditions.

EXPERIMENTAL

Wafers were monocrystalline, sulfur-doped, n-type indium phosphide (n-InP) grown by the liquid-encapsulated Czochralski (LEC) method and supplied by Sumitomo Electric. They were polished on one side and had a surface orientation of (100) and a carrier concentration in the range $3–6 \times 10^{18}$ cm^{-3}. Crystallographic orientation was indicated by primary and secondary flats marking the natural {011} cleavage planes of the wafer according the European/Japanese system. The manufacturer identified these planes from the 'dovetail' and 'V-groove' etch patterns revealed by a standard wet chemical etch. Thus, the primary flat was chosen so that the {111} plane intermediate in direction between it and the (100) surface plane is a {111}A plane , *i.e.* In terminated. For convenience we will call the plane of the primary flat an α plane, the secondary flat a β plane and the wafer surface a γ plane. The schematic in Fig. 1 summarizes the various planes and directions.

To fabricate working electrodes, wafers were cleaved into coupons (typically ~5 mm square) along the α and β planes noting their orientation. Ohmic contact was made by alloying indium to the back of a coupon; the back and the cleaved edges were then isolated from the electrolyte by means of a suitable varnish. The electrode area was typically 0.2 cm^2. Prior to immersion in the electrolyte, the working electrode was immersed in a piranha etchant (3:1:1 H_2SO_4:H_2O_2:H_2O) for 4 minutes and then rinsed with deionized water.

Anodization was carried out in 5 mol dm^{-3} aqueous KOH at room temperature in the absence of light using a linear potential sweep at 2.5 mV s^{-1}. A conventional three-electrode cell configuration was used, employing a platinum counter electrode and a saturated calomel electrode (SCE) to which all potentials are referenced. A CH Instruments Model 650A Electrochemical Workstation interfaced to a Personal Computer (PC) was employed for cell parameter control and for data acquisition.

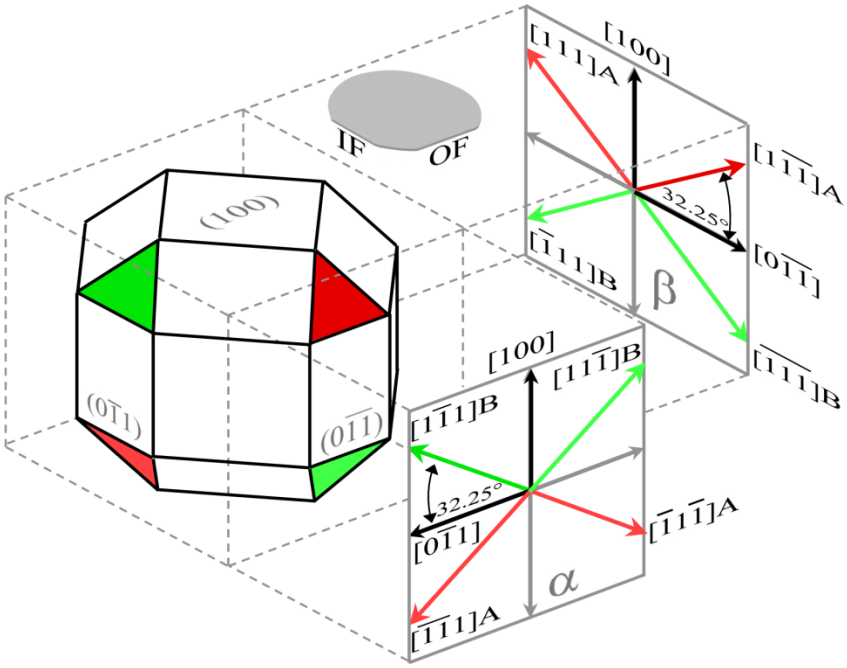


Fig. 1: Isometric drawing showing crystallographic directions and planes relative to the surface and the primary (OF) and secondary (IF) flats of a wafer. We call the primary flat (0$\bar{1}\bar{1}$) an α plane and the secondary flat (0$\bar{1}$1) a β plane. The [1$\bar{1}\bar{1}$]A direction is shown in the β plane and between the [100] and [0$\bar{1}\bar{1}$] directions. This is identified as a [1$\bar{1}\bar{1}$]A direction (*i.e.* In-terminated) from the wafer specification because [100] and [0$\bar{1}\bar{1}$] represent the directions of the surface and primary flats, respectively. Likewise, [1$\bar{1}$1]B is in the α plane and between [100] and [0$\bar{1}$1] as shown.

Cleaved α and β cross sections of electrodes were examined using a Hitachi S-4800 field-emission scanning electron microscope (FE SEM) operating at 5 kV, unless otherwise stated. Electron-transparent sections for plan-view and cross-sectional transmission electron microscopy (TEM) examination were prepared using standard focused ion beam (FIB) milling procedures in an FEI 200 FIB workstation. The TEM

characterization was performed using a JEOL (2000FX and 2011) transmission electron microscope operating at 200 kV.

RESULTS AND DISCUSSION

1. Electrochemical Growth of Nanoporous InP

Fig. 2a shows an LSV of an n-InP electrode in 5 mol dm^{-3} KOH. The potential was scanned at 2.5 mV s^{-1} from an initial potential of 0 V. There is little current at potentials less than 0.3 V, but continued anodization to potentials greater than 0.4 V results in a rapid increase in the current density to a peak value of 20 mA cm^{-2} at 0.48 V. Above 0.48 V, the current density decreases quite rapidly, reaching a value of ~3 mA cm^{-2} at 0.6 V. A significant anodic oxidation process clearly occurs above ~0.4 V and becomes self-limiting at higher potentials. Fig. 2b shows a LSV of a similar n-InP electrode in 1 mol dm^{-3} KOH at the same scan rate (2.5 mV s^{-1}). As in Fig. 2a, an anodic peak can similarly be observed, but at a higher potential (~1.25 V).

The electrodes formed during anodization in the two KOH electrolyte concentrations were examined in TEM. The micrographs shown in Fig. 3 demonstrate that the anodic processes are remarkably different in the two different concentrations of KOH. Fig. 3a shows that anodization in 5 mol dm^{-3} KOH results in the formation of a nanoporous InP layer and it should be noted that similar nanoporous layers were observed in 2 mol dm^{-3} and 3 mol dm^{-3} KOH. Fig. 3a was taken in an under-focus condition and thereby uses phase contrast effects to enhance the visibility of the pores formed within the upper part of the InP. The sense of the Fresnel contrast changes seen as a function of the defocus conditions in through focal series of bright field micrographs confirmed the formation of the low density regions described, although it should be emphasized that the nanopores are heavily interspersed with a high volume fraction of microcrystalline material. Fig. 3b, by comparison, shows that, after a similar potential sweep, there appears to be little change in the electrode during anodization in 1 mol dm^{-3} KOH other than a thin (~25 nm) surface film, as marked at A.

LSVs were performed in 5 mol dm^{-3} KOH over a range of scan rates and in all cases an anodic current peak was observed as in Fig. 2a. While the current densities increase at higher scan rates, the charge density corresponding to the anodic peak was found to remain relatively constant (0.57 C cm^{-2}), indicating that an approximately equal amount of InP is oxidized irrespective of the scan rate.

Further investigation by TEM shows the porous region is capped by a thin layer (~40 nm) close to the surface that appears to be unmodified. The thickness of the nanoporous region is generally uniform although in some areas the interface with the substrate is characteristically non-planar. The average pore width and inter-pore distances are noted to be similar (~40 nm) to one another as well as to the thickness of the near-surface layer.

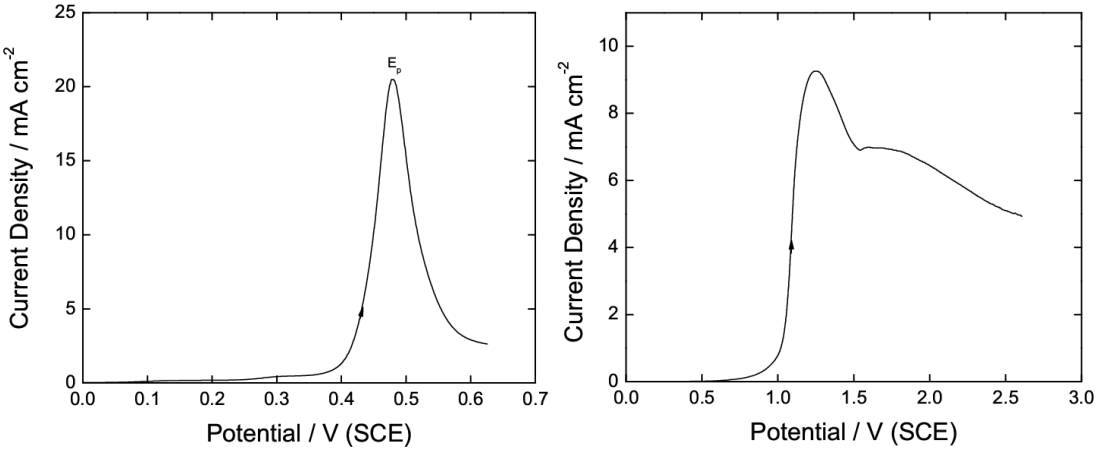


Fig. 2. LSV at 2.5 mV s^{-1} of an n-InP electrode in (a) 5 mol dm^{-3} KOH; (b) 1 mol dm^{-3} KOH.

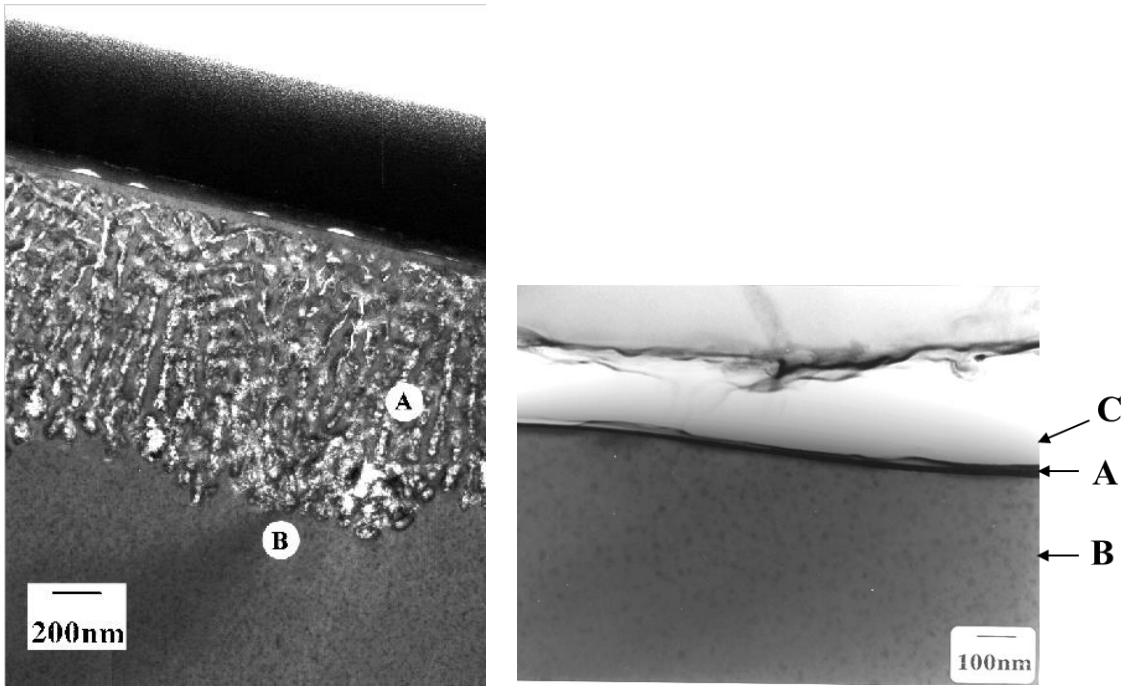
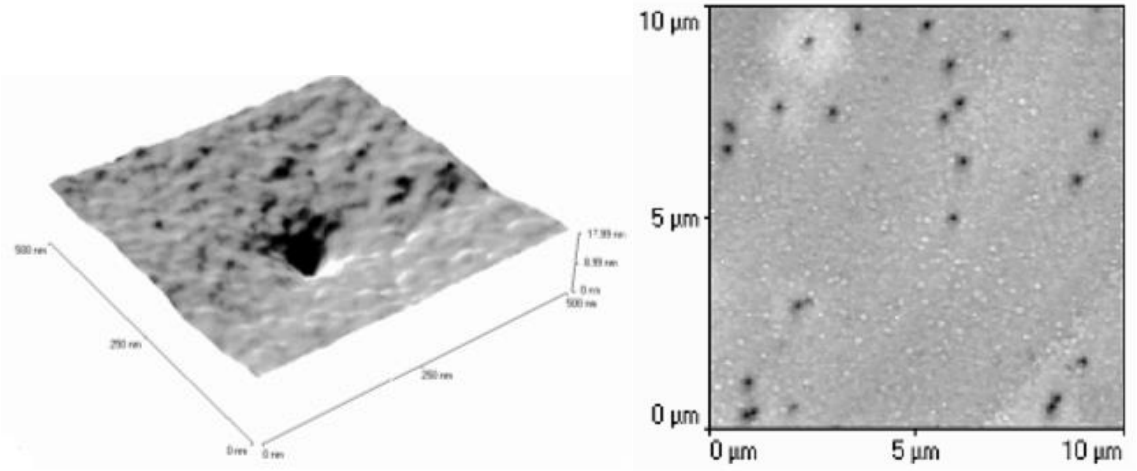


Fig. 3. (a) Under-focus bright field TEM micrograph of an n-InP electrode after an LPS from 0 V to 0.63 V (SCE) at 2.5 mV s^{-1} in 5 mol dm^{-3} KOH. A nanoporous InP layer (A) is observed above the InP substrate (B) and beneath a dense near-surface layer (C). (b) Bright field TEM micrograph of an n-InP electrode cross-section after a LPS from 0 V to 1.3 V (SCE) at 2.5 mV s^{-1} in 1 mol dm^{-3} KOH. A thin surface film (A) is observed above the InP substrate (B). The surface of the sample has been capped by the amorphous deposit marked at C.

The mechanism by which a porous region can form within the substrate by electrochemical oxidation despite the presence of this dense InP layer at the surface at first sight appears to be inconsistent with the microstructure seen in Fig. 3. The near surface region of the anodized InP, however, was found to contain a low volume fraction of localized channels. Evidence for the existence of these channels was obtained from AFM examination of the surface of electrodes after anodization. Electrodes subjected to potential sweep anodization with upper potentials in the range 0.4 V to 0.53 V were also studied by AFM. Fig. 4 shows AFM images of the surface of an electrode following a potential sweep from 0 V to 0.48 V. The image in Fig. 4(a) clearly shows an etch pit that has formed on the surface. The lower magnification images in Fig 4(b) shows the distribution of these pits on the surface from which estimates were made of the areal density (2.3×10^7 cm^{-2} in this case). It is assumed that both the porous layer and the channels through the near-surface layer are filled with electrolyte, which connects the porous structure with the bulk electrolyte. This enables ionic current to flow and electrochemical oxidation of InP to proceed, thus providing a mechanism by which the porous layer can grow. The channels contained within the near-surface layer can thus be seen to play a critical role in the formation of the nanoporous structure.



(a) (b)

Fig. 4. AFM images of the surface of an InP electrode after a linear potential sweep at 2.5 mV s^{-1} in 5 mol dm^{-3} KOH from 0 V to 0.48 V (SCE).

2. Formation of Porous Domains

Fig. 5 shows a typical SEM image of a cleaved β cross section (*i.e.* parallel to the secondary flat) through an electrode after anodization in KOH. The anodization was terminated in the early stages, before a continuous porous layer had developed. Triangular porous regions are clearly visible. This shows that individual, isolated porous domains form in the early stages of anodization. We have shown[2,3] that each such domain

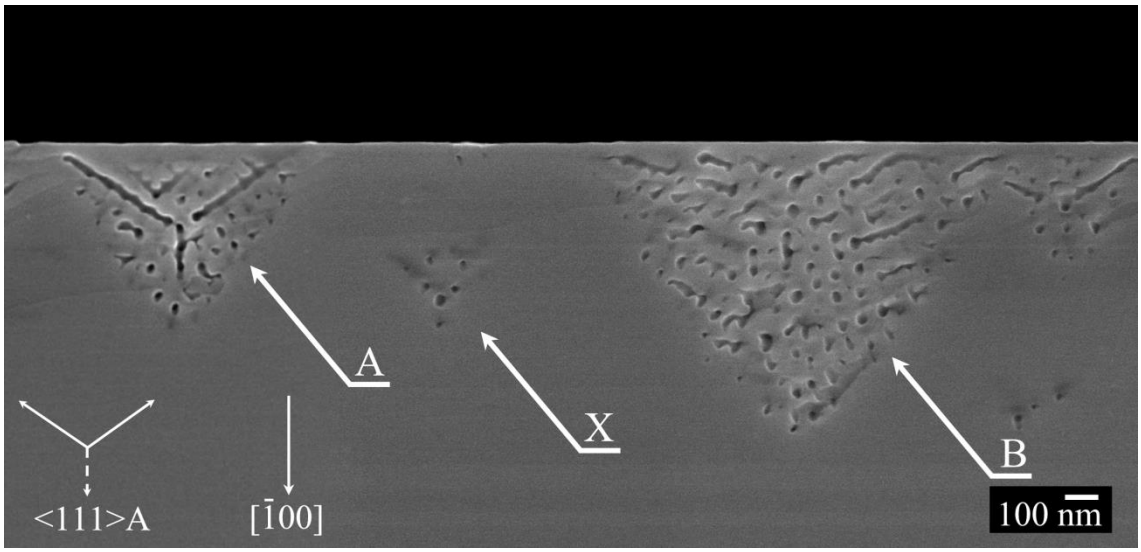


Fig. 5. SEM image of a cleaved β cross section (*i.e.* parallel to the OF flat) of n-InP after an LPS from 0 V to 0.44 V (SCE) in 5 mol dm^{-3} KOH at 2.5 mV s^{-1}. Triangular domain cross sections can be seen at *A* and *B* beneath a thin, non-porous, near-surface layer. Both in-plane pores (line-like features approximately along the <111>A directions shown) and through-plane pores (hole-like features) are evident. The small triangular feature at *X* corresponds to a domain sectioned far from its center as discussed in the text.

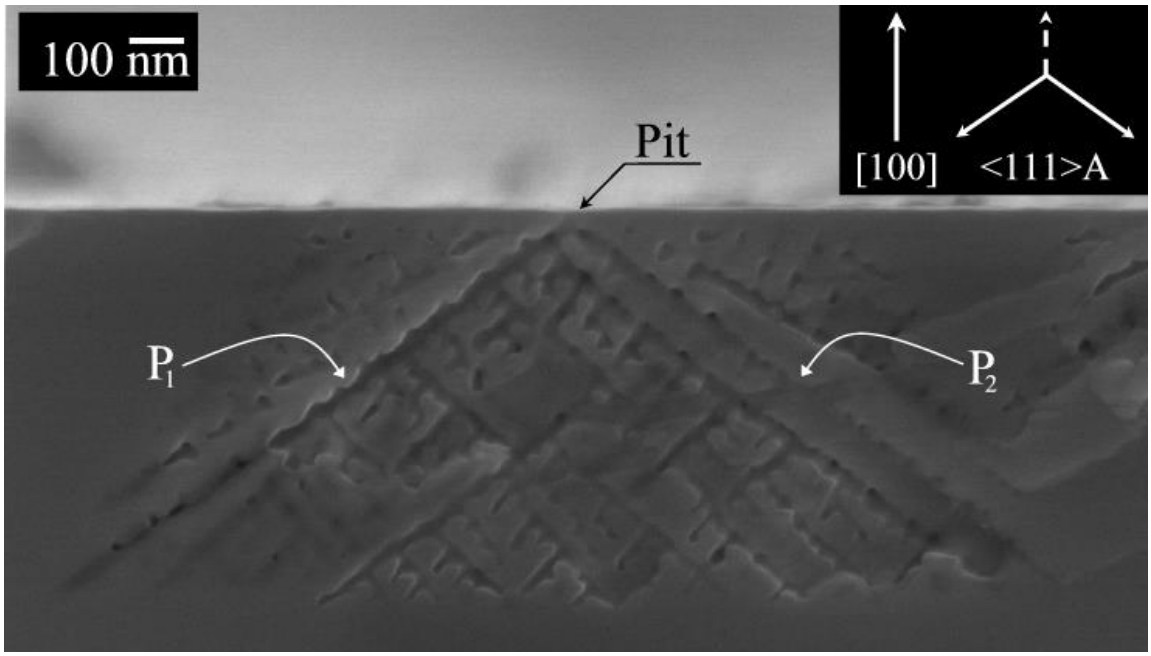


Fig. 6. SEM image of a cleaved α cross section (*i.e.* parallel to the IF flat) of n-InP after anodization under the same conditions as in Fig. 5. A trapezoidal domain cross section can be seen beneath a thin, non-porous, near-surface layer. Both in-plane pores (line-like features approximately along the <111>A directions shown) and through-plane pores (hole-like features) are evident.

is separated from the surface by a thin non-porous layer and is connected to the electrolyte by a pit which penetrates this near-surface layer. Clearly, the β-plane cross sections through these domains are triangular in shape. Most of the pores in Fig. 5 apparently pass through the plane, appearing as hole-like features, but several pores appear to be in the plane.

Fig. 6 shows a typical SEM image of a cleaved α cross section through the same electrode as in Fig 5. A quadrilateral porous region with the shape of a truncated isosceles triangle is observed. Two sides of the quadrilateral are parallel to the surface of the wafer, with the shorter side close to the surface (top). We will refer to this shape as an isosceles trapezoid. Many pores appear along lines in the plane but some pores passing through the plane appear as holes. The center of the trapezoid's short side is connected by a short channel through the near-surface layer to a pit in the surface. From this channel an in-plane pore P_1 extends to the bottom left-hand corner of the trapezoid and another P_2 extends symmetrically to the right. Each of these pores makes an angle of ~35° with the surface and so is along a <111> direction.

As indicated in the experimental section, the {111} plane between the primary flat (α cleavage plane) and the surface (γ plane) of the wafer is a {111}A plane. Likewise the {111} plane between the secondary flat (β cleavage plane) and the surface is a {111}B plane. The corresponding directions (*i.e.* the normal vectors to these planes) are shown schematically in Fig 1. It is clear from Fig. 1 that the <111>A vectors point downwards from the wafer surface in the α planes and upwards towards the wafer surface in the β planes. Thus P_1 and P_2, which originate at the surface and propagate downwards in an α plane, propagate along <111>A directions (as shown in the inset of Fig. 6). Most of the pores in the region below P_1 and P_2 in the image are parallel to P_1 or P_2 while most of the pores above P_1 and P_2 pass through the plane (*i.e.* appear as holes). Revisiting Fig. 5, the pores in the plane of the image also appear to be along <111> directions. These correspond to holes in Fig. 6. Conversely, in-plane pores in Fig. 6 correspond to holes in Fig. 5.

3. Pore Patterns and Shape of Porous Domains

As already discussed, Figs. 5 and 6 suggest that pores are oriented along <111> directions. If pores originating at a surface pit propagated along all eight <111> directions, the domain formed would have the shape of half a cube. However, as already noted, Figs. 5 and 6 show that α and β cross sections are not rectangular. Furthermore, Fig. 6 shows that primary pores propagate along <111>A directions. We therefore suggest that all pores propagate only along the four <111>A directions. This is expected since the fastest etching planes in InP are generally found to be {111}B, *i.e.* the direction of propagation of the etch front is generally <111>A.

The four <111>A directions may be represented by a set of tetrahedrally symmetrical vectors. To model the domain shape that would result from <111>A pore propagation, we first consider the hypothetical case of pores originating from a point in the bulk of the crystal and propagating along four tetrahedrally symmetrical directions (the vectors $\boldsymbol{a}$, $\boldsymbol{b}$, $\boldsymbol{c}$, and $\boldsymbol{d}$) at rates that are equal at any instant in time. After time t, these four pores will have reached points which form the vertices of a tetrahedron. Branching along the <111>A directions from the primary pores will lead to secondary pores and additional branching will lead to tertiary and quaternary pores that fill the volume of the

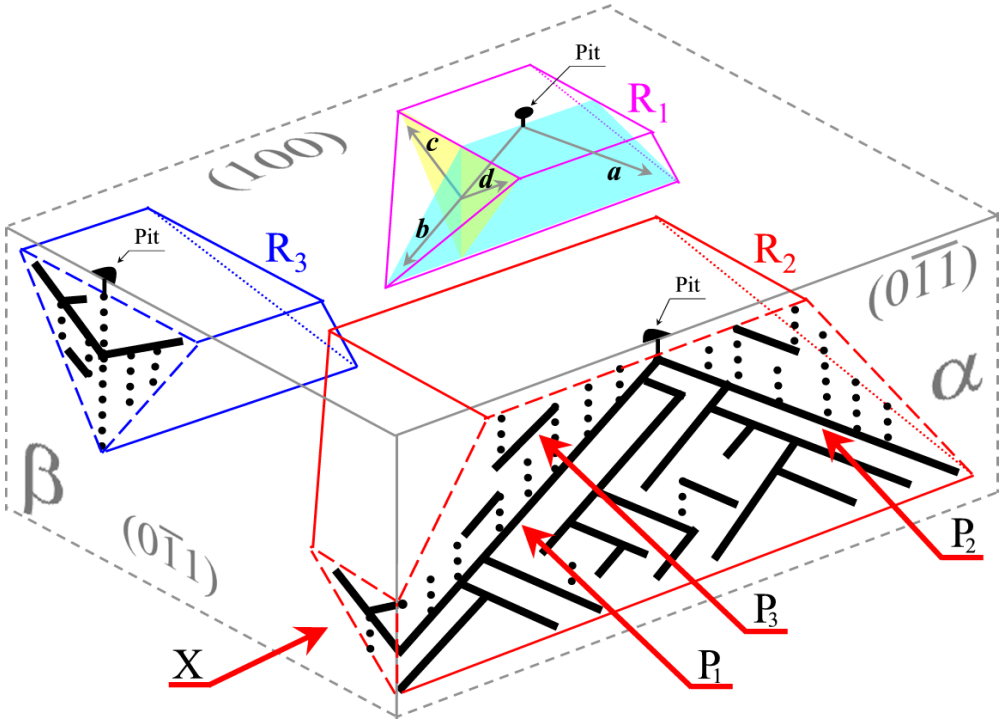


Fig. 7. Schematic of porous domains R_1, R_2 and R_3 beneath a (100) surface and cross sections in the α and β planes. Domains are separated from the surface by a thin layer and each domain originates from a pit penetrating this layer. Pores are represented in R_1 propagating along <111>A directions: downwards along ***a*** and ***b*** in the α plane and upward along ***c*** and ***d*** in the β plane. The α cross section intersects R_2 through its center; the β cross section intersects R_3 through its center and R_2 near its vertex (at X). In the cross sections, in-plane pores are shown as solid lines and through-plane pores as small filled circles. P_1, P_2, and P_3 indicate in-plane α pores.

tetrahedron. Thus, such pore propagation along <111>A directions from a point in the bulk of the crystal would lead to a tetrahedral porous domain.

Of course, pores originate near the surface rather than in the bulk of the crystal and therefore the porous domain formed will have the shape of a tetrahedron truncated by a plane parallel to the surface of the crystal at which the pores originate. The schematic in Fig. 7 shows three such porous domains R_1, R_2 and R_3 beneath a (100) surface (γ plane). It also shows the pit from which the domain has formed in each case and the cross sections in α and β planes. As discussed above, α pores propagate downwards along two of the four <111>A directions ***a*** and ***b***, and β pores branching from these propagate upwards along the other two <111>A directions ***c*** and ***d***. This is shown schematically in R_1. The α cross section shown intersects the domain R_2 through its center forming a trapezoidal shape. Pores originating at the surface pit are shown as solid lines extending downwards in diverging directions to the vertices of the domain. Secondary pores in the plane branch from these primary pores; all pores in the plane are parallel to either ***a*** or ***b***, *i.e.* they are α pores. This is consistent with the SEM image in Fig. 6 where two such primary pores, P_1 and P_2, extend from a surface pit to the lower vertices of the domain and many other pores are observed in the plane branching in directions parallel to P_1 or P_2.

We note that no point in the region between the primary pores (P_1 and P_2) and the surface is accessible by paths involving only α pores because these propagate downwards only. However, β pores can branch from them and propagate upwards towards the surface in the orthogonal (*i.e.* β) planes. Subsequent branching along β directions allows these pores to thread back through the region between the primary pores and the surface. In fact, this is the only way that pores can reach that region. The β pores crossing the α cross section are shown as small filled circles in Fig. 7. Such pores can then branch again to give rise to further α and β pores. This explains the observation that pores above P_1 and P_2 in Fig. 6 mainly pass through the plane (β pores) while pores below P_1 and P_2 are mainly in the plane (α pores). Clearly, the detailed features in Fig. 6 resemble those in the schematic α cross section in Fig. 9 and so are consistent with the model.

The β cross section shown in Fig. 7 intersects the domain R_3 through its center forming a triangular shape as discussed above. Pores in the plane (β pores) are shown as solid lines extending upwards from where the α pores from which they branched cross the plane. Pores propagating upwards in a β plane can branch downwards in several α planes to form in each case a pattern of pores that is generally similar to that in the α cross section shown. These pores appear as holes where they pass through the β cross section and are shown as small filled circles. The detailed features in Fig. 5 resemble the schematic β cross section: pores appear mainly as hole-like images with fewer in-plane pores. The β cross section shown also passes through R_2 but does not intersect its base.

4. A Three-Step Model for Pore Formation

The formation of crystallographically oriented (CO) <111>A pores suggests that etching is controlled by the relative rates of the surface reactions at different facets: any satisfactory model of electrochemical pore formation must explain how this can occur even though the rate-determining process (hole generation) occurs only at pore tips. To reconcile these requirements, we propose a three-step model. The three steps (which are illustrated schematically in Fig. 8) are: (1) hole generation at pore tips, (2) hole diffusion and (3) electrochemical oxidation of the semiconductor to form etch products.

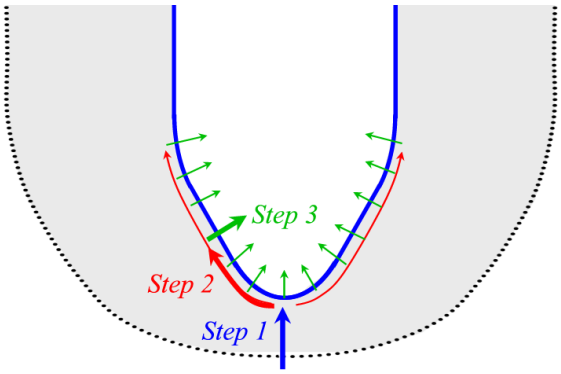


Fig. 8. Schematic representation (not to scale) of a pore near its tip showing the three steps of the model of competitive kinetics: (Step 1) hole generation at pore tips by tunneling of carriers (holes) across the depletion layer (shaded region); (Step 2) hole diffusion at the surface; and (Step 3) electrochemical oxidation of the semiconductor to form etch products.

Step 1 is the generation of holes at pore tips. As discussed above, this is rate-determining and occurs under the influence of a high electric field due to the small radius of curvature at the pore tip. If each hole formed were to be immediately consumed in an electrochemical reaction, then the resulting etching would be confined to a very small area at the pore tip. This would tend to further sharpen the pore tip and therefore further hole generation and etching reaction would also be confined to that specific site. The

question therefore arises as to how pore propagation can occur preferentially along crystallographic directions if the rate-determining step occurs at a non-crystallographically defined site *i.e.* the pore tip.

The answer must lie in Step 2: hole diffusion. If holes diffused only a negligible distance, etching would be confined to the site on the surface where they were created. However, when holes may diffuse parallel to the surface of the semiconductor, the electrochemical etching reaction may occur some distance from the pore tip where the holes are created and, as discussed below, this may lead to CO pore formation. Such diffusion of holes from their points of generation to the points where etching ultimately occurs has been reported[25] for photoanodic etching of n-type III-V semiconductors where etching was observed to extend beyond the illuminated region.

Step 3 is the actual electrochemical reaction itself. While the detailed chemistry and mechanism of this have not yet been elucidated, it involves oxidation of InP to indium and phosphorus species dissolved in the electrolyte within a pore. The kinetics of Step 3 do not determine the overall etch rate of a pore: this is determined by the rate of generation of holes at the pore tip (Step 1). However, competition in kinetics between hole diffusion (Step 2) and electrochemical reaction (Step 3) is the principal factor determining the average diffusion distance of holes.

If the kinetics of Step 3 (oxidation reaction) are slow relative to Step 2 (diffusion), then holes can diffuse a significant distance before being annihilated in the oxidation reaction. Then etching can occur at preferred crystallographic sites, such as phosphorus dangling bonds in InP, within a zone in the vicinity of the pore tip and will lead to pore propagation in preferential directions. On the other hand, if the kinetics of Step 3 were fast relative to Step 2, the diffusion distance of holes would be short as they would be annihilated in the oxidation reaction close to where they were created. In that case, etching would occur close to the site of hole generation rather than at preferred crystallographic sites and so there would then be no preferred crystal direction for pore propagation.

5. Mechanism of Crystallographic Etching of Pores.

When the kinetics of Step 3 are sufficiently slow that holes can diffuse to crystallographically preferred reaction sites, etching will eventually reveal the slowest etching crystal facets – the {111}A facets – to form a pyramidal shape with its apex as the pore tip, as shown in Fig. 9. These {111}A planes are terminated by indium atoms, each bonded to three underlying phosphorous atoms. Removal of an indium atom therefore exposes three phosphorous atoms, each with a dangling bond as shown in Fig. 10a. Such a phosphorus atom is easily etched, breaking a bond to each of three indium atoms, two of which are surface atoms. Each of these now has two dangling bonds (each already had one) and consequently is easily etched, revealing two new phosphorous atoms, each with a dangling bond.

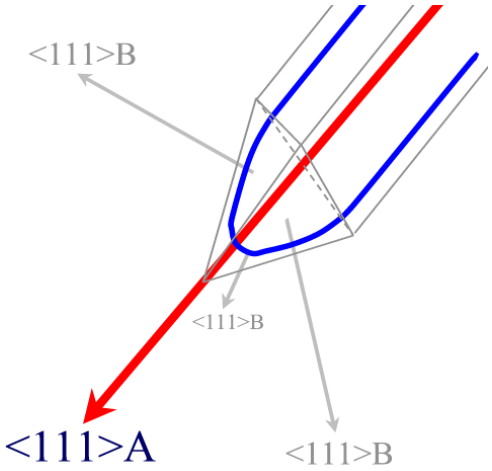
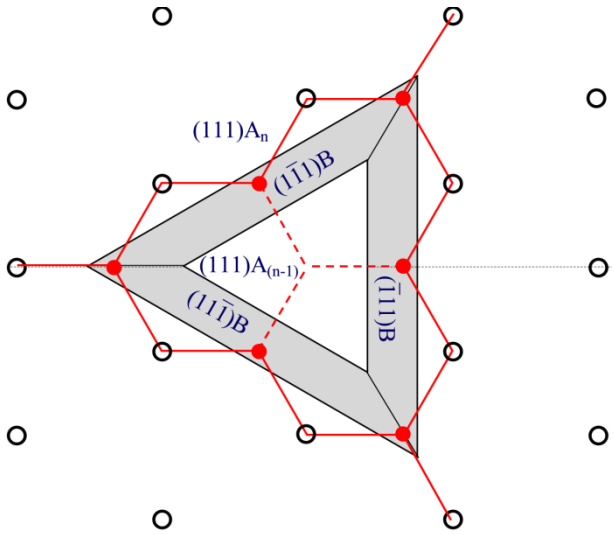
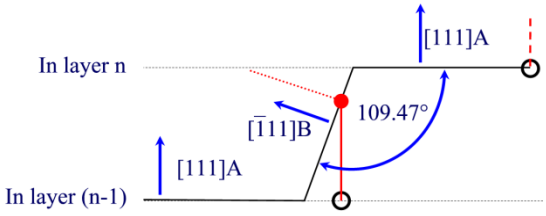


Fig. 9. Schematic representation (not to scale) of a pore formed by the etching mechanism described in Fig. 8. The idealized shape with three {111}A facets is represented by grey lines (_____). The actual pore (represented by blue lines (_____) will have finite radius of curvature at the tip and will generally have rounded pore walls.



(a)



(b)

Fig. 10. (a) An In vacancy (- -)on a {111}A surface creating three dangling P bonds (_ _ _ _). These P atoms (●) correspond to a {111}B monatomic ledge on three sides of the vacancy (projections of which on the {111}A plane are shown). Indium atoms are shown as open circles (○). (b) Cross-sectional view orthogonal to the surface {111}A plane and through the In vacancy and one of the P atoms in a plane containing its dangling bond. The surface {111}A plane (n) and the next underlying {111}A plane (n-1) are shown. The {111}B ledge is represented at an angle of 109.47° to the surface plane and contains the P atom with its dangling bond towards the In vacancy and normal to the surface of the ledge. Note that the P atom is bonded to an In atom in the n-1 plane; as can be seen in (a) it is also bonded to two In atoms in the n plane.

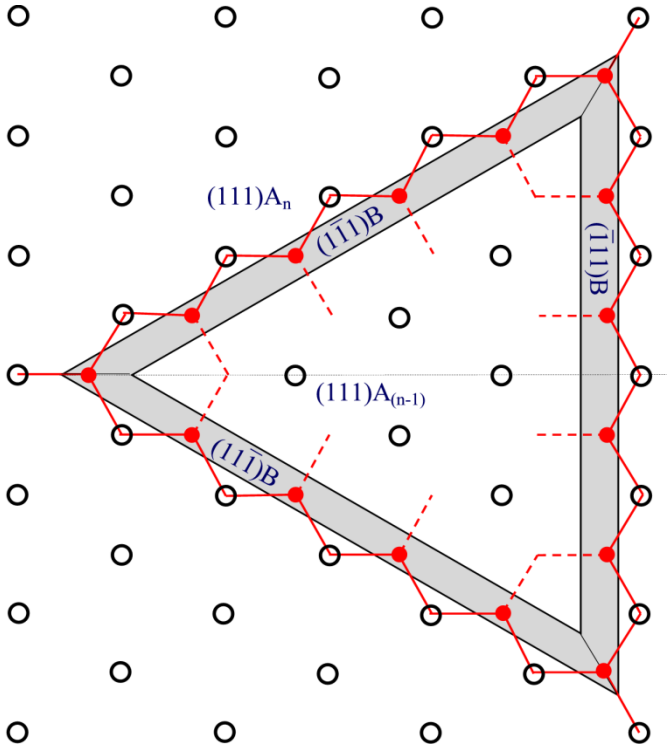


Fig. 11. Expanded three-sided region as etching progresses further away from the original In vacancy shown in Fig. 10. This occurs as follows: as the P atoms on the ledges in Fig. 5a are etched, In atoms with two dangling bonds are exposed which in turn etch. The corner P atoms (which originally had no dangling bonds) are then exposed and etch. Thus each ledge advances to the next row of P atoms.

Phosphorous atoms with single dangling bonds can be considered to be part of a {111}B surface oriented normal to the bonds.[26] Thus, the removal of a single indium atom from a {111}A surface creates three monatomic ledges with {111}B faces, each at an angle of 109.47° to the surface as shown in Fig. 10b. Etching of the phosphorous atoms on these ledges, and the associated indium atoms, causes the ledges to advance, consequently increasing the size of the three sided region where the next underlying {111}A plane is exposed (Fig. 11).

New vacancy sites are not formed easily but, once formed, they expand as in Fig 11 by rapid two-dimensional etching along the surface to expose the next {111}A plane. Eventually, an indium vacancy forms in the newly exposed {111}A face and the etching process continues to expose the next underlying {111}A plane (see Fig. 10). Thus, in the vicinity of the pore tip, the {111}A faces are etched, one monolayer at a time, so that the tip region maintains its pyramidal shape, and so remains sharp, as it propagates. Symmetrical etching of the three {111}A faces forming the tip causes it to propagate in the (fourth) <111>A direction.

The crystallographic etching that maintains {111]A facets in the vicinity of the tip is controlled by the supply of holes diffusing from the tip. The hole concentration at the surface of the facets decreases with distance from the tip, both because of divergence of the diffusing flux and because of consumption of holes in the oxidation reaction. Thus, at some distance from the tip the rate of etching becomes negligibly small. At intermediate

distances, a transition region from etching to non-etching must therefore exist where propagation of ledges on individual planes ceases and where the surface curves away from the {111}A facets towards the central axis of the pore.

Thus, as a pore etches multiple ledges are propagating outwards from multiple initiation points (indium vacancies) on each of the facets. Where these propagating ledges meet they can form three-sided corners at which the local electric field is sufficiently high that hole generation can occur. These sites can become new pore tips when they develop in locations sufficiently far from the depletion regions around adjacent pores. In this way, branching of pores can occur along any of the <111>A directions.

In summary, the three-step model can explain how the concepts of CO etching and rate control by localized hole generation at pore tips can be reconciled. If Step 3 (oxidation reaction) is sufficiently fast that Step 1 (hole generation) is rate-determining but sufficiently slow in comparison with Step 2 (diffusion) that holes can diffuse a significant distance, then preferential etching of {111}B faces can occur. This leads to the formation of a faceted pore tip which, through etching of {111}A planes one monolayer at a time, will lead to the propagation and branching of pores along <111>A directions.

CONCLUSIONS

Anodization of highly doped (10^{18} cm^{-3}) n-InP in 2 – 5 mol dm^{-3} KOH under potentiostatic or potentiodynamic conditions results in the formation of a nanoporous sub-surface region beneath a thin (typically ~40 nm) dense near-surface layer. LSVs show a pronounced anodic peak, typically at 0.48 V for a 2.5 mV s^{-1} scan in 5 mol dm^{-3} KOH, corresponding to the formation of the porous region. However, no porous regions were formed during anodization in 1 mol dm^{-3} KOH. For upper potentials in the range 0.4 V to 0.53 V, AFM images clearly show etch pit formation on the surface.

Detailed TEM and SEM studies show that pores originate from surface pits and an individual, isolated porous domain is formed beneath each pit in the early stages of anodization. Each such domain is separated from the surface by a thin non-porous layer and is connected to the electrolyte by its pit, which penetrates this near-surface layer. Pores emanate from these points along the <111>A crystallographic directions to form domains with the shape of a tetrahedron truncated symmetrically through its center by a plane parallel to the surface of the electrode. Cross sections of these domains are trapezoidal and triangular, respectively, in the α and β cleavage planes of the wafer. The observed SEM and TEM cross sections show pore patterns that are in good agreement with those predicted.

We propose a three-step model of electrochemical pore formation that explains how crystallographically oriented etching can occur even though the rate-determining process (hole generation) occurs only at pore tips. Step 1 is the generation of holes at pore tips under the influence of a high electric field due to the small radius of curvature at the pore tip. Step 2 is the diffusion of holes parallel to the surface of the semiconductor, enabling the electrochemical etching reaction to occur some distance from the pore tip where the holes are created. Step 3 is the actual electrochemical reaction itself.

Step 1 determines the overall etch rate. However, competition in kinetics between hole diffusion (Step 2) and electrochemical reaction (Step 3) determines the average diffusion distance of holes and this in turn determines whether etching is crystallographic. If the kinetics of Step 3 are slow relative to Step 2, then etching can

occur at preferred crystallographic sites, such as phosphorus dangling bonds in InP, within a zone in the vicinity of the pore tip and this will lead to pore propagation in preferential directions.

Under these conditions, etching will eventually reveal the slow etching {111}A facets to form a pyramidal pore tip. Indium vacancy sites formed on these facets expand by rapid two-dimensional etching along the surface to expose the next {111}A plane. Thus, in the vicinity of the pore tip, the {111}A faces are etched, one monolayer at a time, so that the tip region maintains its pyramidal shape, and so remains sharp, as it propagates. Symmetrical etching of the three {111}A faces forming the tip causes it to propagate in the (fourth) <111>A direction. As a pore etches, propagating atomic ledges can meet to form sites that can become new pore tips and this enables branching of pores along any of the <111>A directions.

Acknowledgements

R. P. Lynch and N. Quill would like to thank the Irish Research Council (IRC) for PhD scholarships to perform this research. R. P. Lynch acknowledges a joint IRC - Marie Curie Fellowship under grant no. INSPIRE PCOFUND-GA-2008-229520. The authors would also like to acknowledge the support of the Tyndall National Institute. This support was provided through the SFI-funded National Access Programme (Project NAP No. 37 and 70). The authors also acknowledge many contributions to the electron microscopy by S. B. Newcomb and to the AFM measurements by M. Serantoni.

REFERENCES

1. R.P. Lynch, N. Quill, C. O'Dwyer, S. Nakahara and D.N. Buckley, *Phys. Chem. Chem. Phys.*, **15**, 15135-15145 (2013)
2. R.P. Lynch, C. O'Dwyer, N. Quill, S. Nakahara, S.B. Newcomb, and D.N. Buckley, *J. Electrochem. Soc.*, 160, D260-D270 (2013).
3. C. O'Dwyer, D.N. Buckley, D. Sutton, M. Serantoni, and S.B. Newcomb, *J. Electrochem. Soc.*, **154**, H78 (2007)
4. C. Fang, H. Föll, J. Carstensen and S. Langa, *phys. stat. sol. (a)* **204** (5), 1292 (2007)
5. C. O'Dwyer, D.N. Buckley, D. Sutton, and S.B. Newcomb, *J. Electrochem. Soc.*, **153,** G1039 (2006)
6. C. Fang, H. Föll and J. Carstensen, *J. Electroanal. Chem.* **589**, 259 (2006)
7. J.J. Kelly and H.G.G. Philipsen, *Curr. Opin. Solid-State Mater. Sci.* **9**, 84 (2005)
8. S. Langa, J. Carstensen, I.M. Tiginyanu, M. Christopersen and H. Föll, *Electrochem. Solid-State Lett.* **4,** G50 (2001)
9. M. Christopherson, J. Carstensen, S. Rönnebeck, C. Jäger, W. Jäger, and H. Föll, *J. Electrochem. Soc.*, **148**, E267 (2001)
10. D.J. Lockwood, P. Schmuki, H.J. Labbé, J.W. Fraser, *Physics E*, **4**, 102 (1999)
11. T. Osaka, K. Ogasawara and S. Nakahara, *J. Electrochem. Soc.*, **144**, 3226 (1997)
12. A.G. Cullis, L.T. Canham and P.D.J. Calcott, *J. Appl. Phys.*, **82**, 909 (1997)
13. M. Schoisswohl, J.L. Cantin, M. Chamarro, H. J. von Bardelben, T. Morganstern, E. Bugiel, W. Kissinger and R.C. Andreu, *Phys. Rev. B*, **52**, 11898 (1995)
14. B.H. Erné, D. Vanmaekelbergh, J. J. Kelly, Adv. Mater., 7, 739 (1995)

15. T. Takizawa, M. Nakahara, E. Kikuno and S. Arai, J. Electron. Mat., 25, 657 (1996)
16. S. Langa, J. Carstensen, M. Christophersen, K. Steen, S. Frey, I.M. Tiginyanu and H. Föll, *J. Electrochem. Soc.* **152**, C525 (2005)
17. N. Quill, R. P. Lynch, C. O'Dwyer, D. N. Buckley, *ECS Trans.,* **50(37)**, 143 - 153 (2013) *doi:10.1149/05037.0143ecst*
18. H. Fujikura, A. Liu, A. Hamamatsu, T. Sato and H. Hasegawa, Jpn. J. Appl. Phys. 39, 4616 (2000)
19. S. Langa, I.M. Tiginyanu, J. Carstensen, M. Christopersen and H. Föll, *Electrochem. Solid-State Lett*, **3**, 514 (2000)
20. F.M. Ross, G. Oskam, P.C. Searson, J.M. Macaulay and J.A. Liddle, *Philos. Mag. A* **75**, 525 (1997)
21. H. Tsuchiya, M. Hueppe, T. Djenizian and P. Schmuki, *Surf. Sci.* **547,** 268 (2003)
22. X. G. Zhang, *J. Electrochem. Soc.,* **151**, C69 (2004)
23. S.N.G. Chu, C.M. Jodlauk and W.D. Johnston, Jr., *J. Electrochem. Soc.* **130**, 2399 (1983)
24. D. Soltz and L. Cescato, *J. Electrochem. Soc.* **143**, 2815 (1996)
25. F. W. Ostermayer, P. A. Kohl, R. M. Lum, *J. Appl. Phys.,* **58**, 4390 (1985)
26. D. N. MacFayden, *J. Electrochem. Soc.,* **130**, 1934 (1983)